

# Suzaku Metal Abundance Patterns in the Outflow Region of M82 and the Importance of Charge Exchange

Saori KONAMI,<sup>1,2</sup> Kyoko MATSUSHITA,<sup>1</sup> Takeshi Go TSURU,<sup>3</sup> Poshak GANDHI,<sup>4</sup>  
 and Toru TAMAGAWA<sup>2,1</sup>

<sup>1</sup> Department of Physics, Tokyo University of Science, 1-3 Kagurazaka, Shinjuku-ku, Tokyo 162-8601

<sup>2</sup> High Energy Astrophysics Laboratory, the Institute of Physical and Chemical Research, 2-1 Hirosawa, Wako, Saitama 351-0198

*konami@crab.riken.jp*

<sup>3</sup> Department of Physics, Kyoto University, Kitashirakawa-oiwake-cho, Sakyo-ku, Kyoto 606-8502

<sup>4</sup> Institute of Space and Astronautical Science (ISAS), Japan Aerospace Exploration Agency, 3-1-1 Yoshinodai, Chuo-ku, Sagami-hara, Kanagawa 252-5210

(Received ; accepted )

## Abstract

We performed spectral analysis of Suzaku data of the galactic disk and outflow regions of the starburst galaxy M82. Thermal modeling of the central disk regions requires at least three temperature components. The  $\text{Ly}\beta$  line fluxes of O VIII and Ne X exceed those expected from a plasma in collisional ionization equilibrium. The ratios of  $\text{Ly}\beta/\text{Ly}\alpha$  lines for O VIII and Ne X are higher than those of collisional ionization equilibrium, which may be caused by the process of charge exchange. In the outflow wind region, the spectra are well reproduced with two-temperature thermal models, and we have derived the metal abundances of O, Ne, Mg, and Fe in the outflow. The ratios of O/Fe, Ne/Fe, and Mg/Fe are about 2, 3, and 2, respectively, relative to the solar value determined by Lodders (2003). Since there is no evidence of charge exchange in outflow region, the metal abundances should be more reliable than those in the central region. This abundance pattern indicates that starburst activity enriches the outflow through SN II metal ejection into intergalactic space.

**Key words:** galaxies: individual (M 82), galaxies: interstellar medium, galaxies: abundances, galaxies: starburst, X-rays: galaxies

## 1. Introduction

Metals in hot gas in the interstellar medium (ISM) and intergalactic medium can provide a cumulative fossil record on the history of star formation and evolution of galaxies. Starburst galaxies play an important role in supplying intergalactic metals via outflows heated by type II supernovae (SN II). These outflows are thought to contain metals synthesized by SN II and may have enriched the intra-cluster medium (ICM) and warm-hot intergalactic medium (WHIM).

Recent X-ray observations of starburst galaxies have revealed extended halos of hot plasma around several galaxies (e.g. Wang et al. 2005; Strickland 2007; Wang et al. 2009). However, measurements of metal abundances within these outflows are limited. For NGC 253, XMM-Newton detected the metals O, Ne, Mg, Si, and Fe in the central regions  $\lesssim 3$  kpc along the outflow axis (e.g. Bauer et al. 2007). For NGC 4631 the abundance patterns for O, Ne, Mg, Si and Fe were observed in the extended halo region,  $\sim 13$  kpc with Suzaku (Yamasaki et al. 2009). The outflow wind and disk regions of NGC 4631 show patterns close to those expected from the SN II yields and solar abundance (Lodders 2003), respectively.

M 82 is the most famous, prototypical starburst galaxy with an X-ray emitting outflow (e.g. Tsuru et al. 1997;

Stevens et al. 2003; Origlia et al. 2004). Tsuru et al. (1997) observed M 82 with ASCA and derived a peculiar abundance pattern of O/Ne/Mg/Si/S and Fe in the hot X-ray emitting plasma around the starburst region. No combination of SN Ia and SN II could reproduce the observed abundance pattern. Furthermore, Ranalli et al. (2008) reported spatial variations of the abundances with XMM-Newton. They found the abundances of O, Ne, Mg, Si, and Fe to increase from the center going out to the external outflow region, the absolute value of the O abundance they found was extremely low. In contrast, Tsuru et al. (2007) derived SN II like abundance pattern in the ‘cap’ region, which may be a large photoionized cloud in the halo of M82, at a distance of 11.6 kpc north from the center.

Lallement (2004) has pointed out that line emission in the ‘cap’ region could arise from the process of charge-exchange (CX), where highly ionized gas may be colliding with the cold cloud. Tsuru et al. (2007) reported that an emission line consistent with the C VI transition of  $n = 4$  to 1 at 0.459 keV has been marginally detected, although it is not statistically significant at the 99% confidence level; the presence of this line would suggest charge-exchange processes in the ‘cap’ region with Suzaku. In the XMM spectra in the central region, Ranalli et al. (2008) reported line-like features around  $\sim 0.7$  keV and 1.2 keV, which

were interpreted as CX reactions of neutral Mg and Si, respectively. Most recently, in the XMM reflection grating spectra (RGS), Liu et al. (2011) reported detection of the CX emission of O VII, Ne IX, and Mg XI triplets at the center region. An important piece of evidence of CX is that the forbidden lines are stronger than the resonance lines, especially for O VII ions. They concluded that a significant fraction of these lines originate as a result of CX emission rather than thermal radiation.

CX occurs between highly ionized atoms and neutrals, and emits X-ray emission lines. When a highly ionized ion hits a neutral atom, an electron is captured in an excited state in the ion. It then decays to the ground state, emitting X-ray photons. CX emission has been detected from regions where hot and cool gas co-exist. The first discovery of CX was from comet Hyakutake (Lisse et al. 1996), following which X-ray emission was detected from many comets. More recently, the diffuse soft X-ray background was found to contain CX emission from neutrals in the geocorona/heliosphere and solar wind ions (e.g. Cox 1998; Cravens 2000). In studies of supernova remnants, CX emission can explain anomalously high intensity ratios (i.e.  $\beta/\alpha$  and  $\gamma/\alpha$  lines) compared with those of collisional ionization equilibrium (CIE) plasma (Rasmussen et al. 2001, Katsuda et al. 2011). In the M 31 bulge, an intensity excess at the O VII triplet was observed owing to CX emission (Liu et al. 2010).

Over the 3 keV energy range in the spectra of M 82, there are hard components whose nature is not yet fully understood. Some part of this emission comes from point sources (X-1, for example; Miyawaki et al. 2009). With Chandra and XMM-Newton, Strickland & Heckman (2007) detected diffuse hard X-ray emission and Fe-K line emission which cannot be attributed to CIE plasma.

In this paper, we investigated the spatial distribution of abundance patterns in the outflow wind of M 82, between the center and the ‘cap’ regions. We also derived ratios of  $K\beta$  to  $K\alpha$  lines of O and Ne and studied the spatial variation of the effect of CX emission. We expect both hot ions and cold atoms exist in the center and the ‘cap’ regions. This paper is structured as follows. In section 2, we summarize observations of Suzaku and XMM-Newton. Sections 3 and 4 detail the data analysis and results. Section 5 gives a discussion of these results. Finally, in section 6 we present our conclusions.

We adopted 3.53 Mpc for the distance to M 82, which was determined by the luminosity of the tip of red giant branch (Karachentsev et al. 2004). Unless noted otherwise, we use the new solar abundances in Lodders (2003), and the quoted errors are for a 90% confidence interval for a single interesting parameter.

## 2. Observation and Data Reduction

### 2.1. Suzaku

Suzaku observed M 82 on three occasions in 2005 October during the Science Working Group phase to investigate the outflowing hot gas from the galactic plane. The logs of three observations are listed in table 1. The

XIS consists of three front-illuminated (FI: XIS0, XIS2 and XIS3) CCD cameras and one back-illuminated (BI: XIS1) CCD camera (Koyama et al. 2007). Combined with XRT (Serlemitsos et al. 2007), the field of view (FOV) of the XIS covers a  $\sim 18' \times 18'$  region with a half-power diameter (HPD) of  $\sim 2'$ . The XIS was operated in normal clocking mode (8 s exposure per frame), with the standard  $5 \times 5$  and  $3 \times 3$  editing mode. We processed the XIS data using the “xispi” and “makepi” ftool tasks and CALDB files of version 2009-08-13. The XIS data were then cleaned by assuming thresholds on the Earth elevation angle of  $> 5^\circ$  and the Day-Earth elevation angle of  $> 20^\circ$ . We also discarded data with time since south Atlantic anomaly passage of less than 436 sec. After this screening, the remaining good exposure was 101.1 ksec for both FIs and BI summed over the three observations. Event screening with cut-off rigidity was not performed.

The spectral analysis was performed with HEASoft version 6.10 and XSPEC 12.6. To subtract the non-X-ray background (NXB), we employed the Dark-Earth database using the “xisnxbgen” ftool task (Tawa et al. 2008). We generated two different ancillary response files (ARFs) for the spectrum of each region; one assumed uniform sky emission, while the other utilized the observed XIS1 image by the “xissimarfgn” ftool task (Ishisaki et al. 2007). In the ARFs, we also included the effect of contamination on the optical blocking filters (OBF) of the XIS.

### 2.2. XMM-Newton

As mentioned in Tsuru et al. (2007), since there is a luminous point source within the outflow of M 82, we analyzed the XMM-Newton data to estimate its contamination. Although XMM-Newton observed M 82 four times, we analyzed the data from 2004 April. This observation has the single largest exposure time, which is sufficient for this analysis. The log of this observation is given in table 1. The European Photon Imaging Camera (EPIC), aboard XMM-Newton, has two metal oxide semiconductor (MOS) CCD arrays and one PN CCD array. All three cameras have a  $\sim 30'$  diameter circle FOV with a HPD of  $\sim 6''$ , which is much smaller than the XRT and hence advantageous for observations of point sources.

All data were processed using version 10.0.0 of the XMM-Newton Science Analysis Software (SAS). Periods with a 10–15 keV background count rate deviating by more than  $3\sigma$  from the mean rate were filtered out. The resultant exposure times are also listed in table 1.

## 3. Analysis and Results for the Disk region

### 3.1. Extraction Regions of Spectra

Figure 1 (a) shows the Suzaku X-ray image in energy range of 0.3–2 keV range, along with the spatial regions used for spectral analysis. We defined the square region within  $3' \times 12'$  of the center of M 82 as Disk region. Moreover, because there may be spatial variations in abundance patterns (Ranalli et al. 2008), the region between Disk and ‘cap’ were divided into three regions

**Table 1.** Logs of Suzaku and XMM-Newton observations

Instrument	Observation ID	Observation Start Date	Effective Exposure (ks)
XIS	100033010	2005/10/04	32.3
	100033020	2005/10/19	40.4
	100033030	2005/10/27	28.4
EPIC	0206080101	2004/04/21	66.8/68.2/52.9*

\* The exposure times of the MOS1/MOS2/PN.

as shown in figure 1 (a). These three regions are labeled Wind-1, Wind-2, and Wind-3 in order, from the center. In this paper, we derived abundance patterns of these regions. The three regions outside the M 82 wind are selected to extract background emission, and are shown as green ellipses (figure 1 (a)). We added the spectra of these three regions in order to derive the background spectra.

In the figure 1 (b), we show the XMM-Newton EPIC image in 0.3–5 keV range, overlaid with the extraction regions for Suzaku. As mentioned in Tsuru et al. (2007), the luminous X-ray source in the outflow lies in the region Wind-3, and we refer to it as Source A, hereafter.

### 3.2. Fitting the Spectra

We fitted the Disk region spectra with following model:  $\text{phabs}_{\text{M82}} \times \text{vapec}_{1\text{T}, 2\text{T}, \text{ or } 3\text{T}} + \text{phabs}_{\text{X-1}} \times \text{cutoff PL}_{\text{X-1}}$ . The  $\text{phabs}_{\text{M82}}$  and  $\text{phabs}_{\text{X-1}}$  factors represent the column density. The first of these is left free and the second one is fixed to  $1.1 \times 10^{22} \text{ cm}^{-2}$  (Miyawaki et al. 2009). The ISM emission of M 82,  $\text{vapec}_{1\text{T}, 2\text{T}, \text{ or } 3\text{T}}$ , was represented by one-temperature (1T), two-temperature (2T), and three-temperature (3T) models, employing the vapec plasma code (Smith et al. 2001). We divided the metals into the groups of O, Ne, (Mg & Al), Si, S, (Ar & Ca) and (Fe & Ni) based on the metal synthesis mechanism of SN, and allowed each group to vary. In the 2T or 3T modeling, the vapec components were assumed to share the same elemental abundances. Because our purpose is to derive metal abundance of CIE hot plasma, we accepted the best fit absorbed cutoff power-law (PL) model from Miyawaki et al. (2009) for the hard component, which is dominated by emission from X-1. The cutoff energy is fixed to 5.8 keV, which is the best-fit value in Miyawaki et al. (2009). Meanwhile, the photon index and normalization are set free. We simultaneously fitted the spectra of all CCDs, using the energy ranges of 0.4–6 keV for the BI CCD and 0.5–6 keV for the FI CCDs. Because there are known calibration issues of the Si edges in all CCDs, the energy range of 1.84–1.86 keV is ignored, hereafter (Koyama et al. 2007).

The 1T, 2T, and 3T models failed to reproduce the spectra,  $\chi^2/\text{d.o.f.} = 2376/942$ ,  $1784/940$ , and  $1673/938$  respectively, despite improving fit statistic values. There are large residuals around 0.5–0.7 and  $\sim 1.2$  keV as shown in top of figure 2. Although we tested fits with 4T and 5T models, the residuals features and fit statistics do not change significantly,  $\chi^2/\text{d.o.f.} = 1647/936$  and  $1653/934$ ,

respectively. Therefore, we treated thermal components represented by 3T models. The large residuals existing around 0.5–0.7 and  $\sim 1.2$  keV correspond to O VII/VIII and Ne X Ly $\beta$  emission lines, respectively. We considered that these highly ionized O and Ne may occur CX interacting with neutrals. Adding six gaussians to represent O and Ne emission lines at 0.574 keV (O VII K $\alpha$ ), 0.66 keV (O VII K $\beta$  + O VIII Ly $\alpha$ ), 0.774 keV (O VIII Ly $\beta$ ), 0.921 keV (Ne IX K $\alpha$ ),  $\sim 1.02$  keV (Ne IX K $\beta$  + Ne X Ly $\alpha$ ), and  $\sim 1.2$  keV (Ne X Ly $\beta$ ), we fitted the spectra with the above model while setting O and Ne abundance of vapec models to zero. The Gaussian line centers for only 1.02 keV and 1.2 keV are set free, because relatively strong Fe-L line emission exists in this energy ranges. The phabs component is fixed at  $29.9 \times 10^{20} \text{ cm}^{-2}$ , which is value of fitting with 3T models. This model produced a best fit with  $\chi^2/\text{d.o.f.} = 1364/933$  and the derived parameters are listed in table 2.

Although the large residuals disappear with the above fit, the discrepancies of residuals between XIS0 and XIS1 still remain, over the energy range of 0.5–0.7 keV. These residuals were attributed to contamination on the optical blocking filters (OBF) on the XIS. It is known that contaminant has been accumulating on the OBF since the detector doors were opened following launch (Koyama et al. 2007). To estimate the effect of absorption, we added the model ‘varabs’, which treats photoelectric absorption with variable abundances. The parameters of C is set free. Meanwhile, we set O to 1/12 of C in units of the solar ratio, assuming the contaminant material of the OBF to be C<sub>24</sub>H<sub>38</sub>O<sub>4</sub> and owing to the solar units of the abundances in the model. We fitted the spectra with a model of 3T plus gaussians multiplied varabs, which yielded  $\chi^2/\text{d.o.f.}$  of 1293/929. The fitted spectra are shown in the bottom panel of figure 2. The column density of C and O are 2.2–7.8 and  $0.37\text{--}1.33 \times 10^{17} \text{ cm}^{-2}$ , respectively. These values are consistent with those during other early observations (Fujimoto et al. 2007). The derived parameters are listed in table 2. Although the fits are not formally acceptable, these results are useful for assessing whether CX is important or not.

## 4. Analysis and Results for the Wind regions

### 4.1. Contamination of Disk Emission

The Disk emission contaminates the Wind regions owing to the low Suzaku angular resolution (HPD  $\sim 2'$ ). We simulated the emission from the Disk region in each Wind

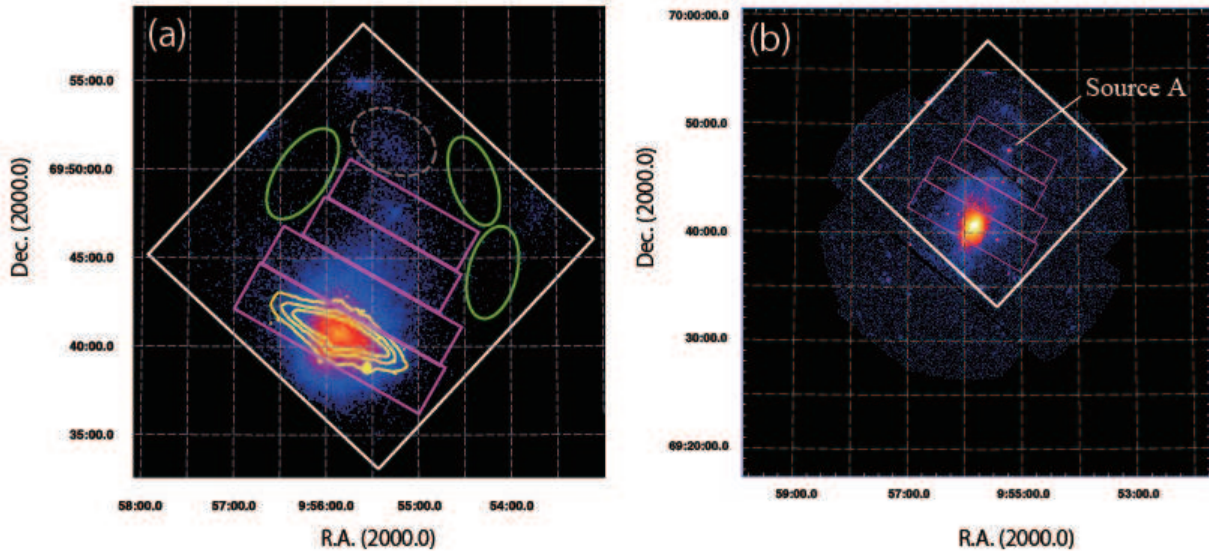


**Fig. 1.** Panel (a) and (b) are the X-ray images of M 82 with the Suzaku XIS1 and XMM-Newton EPIC-MOS1, respectively. The background components were not subtracted and vignetting was not corrected for in these images. Panel (a); the XIS 1 image in 0.3–2 keV is smoothed with a  $\sigma=5.2''$  Gaussian profile and overlaid with optical galactic disk contours from the Digitized Sky Survey (yellow). The magenta boxes show the regions for spectra extraction labeled Disk, Wind-1, Wind-2, and Wind-3 going out from the center. The background spectra were extracted from the three green ellipses. The gray ellipse shows the ‘cap’ region (Tsuru et al. 2007). Panel (b); the selected Wind regions are overlaid. The position of Source A is also indicated. The white box is the Suzaku XIS field of view in both panels.

region, setting the point source to the coordinates of X-1 by `xissimarfgen` in the energy range of 0.2–16 keV, because the Suzaku PSF does not allow us to resolve the X-ray peak of hot ISM and X-1 (Ishisaki et al. 2007). We found a level of 9%, 1%, and 0.5% Disk intensity contamination to the Wind-1, Wind-2, and Wind-3 regions, respectively. The level of contamination is almost constant, to within 5% below 6 keV, and within 20% at 6–10 keV. As shown in figure 3, most of the Wind-1 emission beyond 1.5 keV can be attributed to the Disk region. Meanwhile, in the Wind-2 and Wind-3 regions, the contamination from Disk emission is smaller compared with Wind-1. The intensity of contamination from Disk region is one-half and one-fifth of that in Wind-2 and Wind-3 above  $\gtrsim 1.5$  keV, respectively. Hereafter, we analyze the spectra of Wind-1 and Wind-2 regions after subtraction of the directly-scaled emission of the Disk region. Full statistical error propagation was employed in this analysis.

#### 4.2. Wind-1 Region

We first fitted the Wind-1 region spectra after subtracting 9% of the Disk emission and the background emission accumulated over three background regions with the following model;  $\text{phabs}_{\text{G}} \times \text{vapec}_{2\text{T}}$ . The Wind-1 region spectra will be reproduced as the sum of Disk emission, power-law component of X-1, and Wind-1 emission. The  $\text{phabs}_{\text{G}}$  factor is fixed to  $4.0 \times 10^{20} \text{ cm}^{-2}$ , which is the Galactic value of  $N_{\text{H}}$  in the direction of M 82. The abundances of O, Ne, Mg, and Fe are allowed to vary, and those of other metals are fixed to solar value. We simul-

taneously fitted the spectra of all CCDs over the energy ranges of 0.4–5.0 keV for the BI CCD and 0.5–5.0 keV for the FI CCDs. The 1T and 2T models failed to reproduce the spectra, with  $\chi^2/\text{d.o.f.}=845/305$  and  $807/303$ , respectively. Above 2 keV, there are large negative residuals which we attribute to excess subtraction of the Disk emission contamination.

The simulated intensity of Disk contamination may have some uncertainties due to spatial spread of the X-ray emission and uncertainties in the point spread function. Therefore, we tested the effect of varying the Disk contamination level over 6–8.5%, subtracting off this component, and then carrying out the fit. The  $\chi^2/\text{d.o.f.}$  values are plotted in figure 4, and are found to show a minimum at 354/294 with the contaminant level of 7% of the Disk emission. Above 2 keV, the spectra of the Wind-1 region are well reproduced by the contamination of 7% emission from the Disk region (figure 3), and these parameters were adopted hereafter. The derived parameters and fitted spectra are shown in the first row of table 3 and in figure 5, respectively. As shown in figure 5, in the Wind-1 spectra, several emission lines are detected. The ones around 0.5–0.6 keV, 0.6–0.7 keV and  $\sim 1.3$  keV are identified with  $\text{K}\alpha$  lines of O VII, O VIII, and Mg XI, respectively. The emission bump around 0.7–1 keV corresponds to Fe-L complex, as well as to K-lines from Ne IX and Ne X.

To investigate the sensitivity of metal abundance determination on the ISM temperature, we also employed the 1T and 3T models and fitted the spectrum again, assuming that the Disk contamination level is 7%. The 1T and

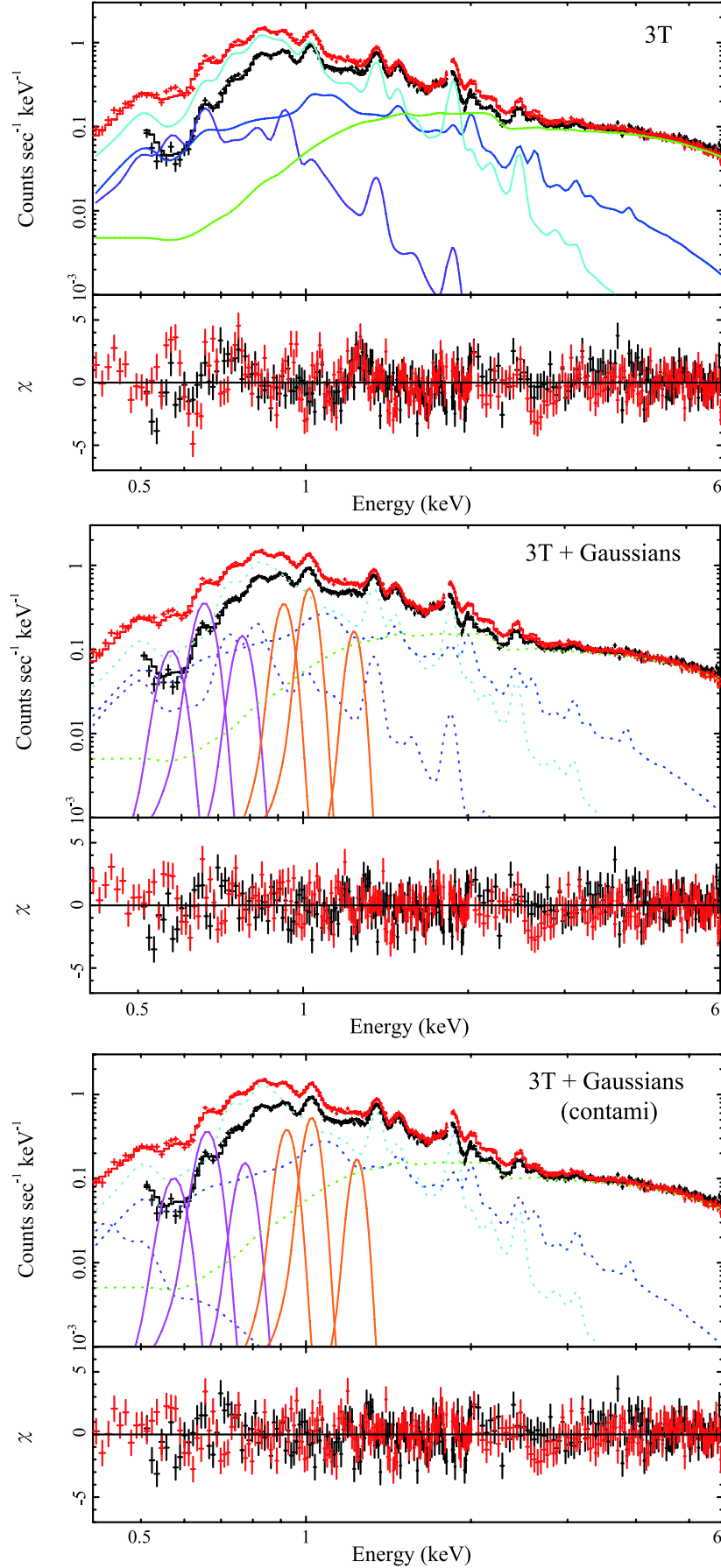


**Fig. 2.** Background-subtracted XIS0 (black) and XIS1 (red) spectra of Disk, shown without removal of the instrumental response. In order from top to bottom, the panels are the spectra fitted with model 3T for ISM, 3T + Gaussian lines, and 3T + Gaussian lines with absorption of OBF contaminant. Black and red lines show the best-fit model in each case for FIs and XIS1, respectively. For simplicity, only the model components plot of the XIS1 spectra are shown. Light blue, blue and purple lines are the three ISM temperature components. Green curves represent the accu-

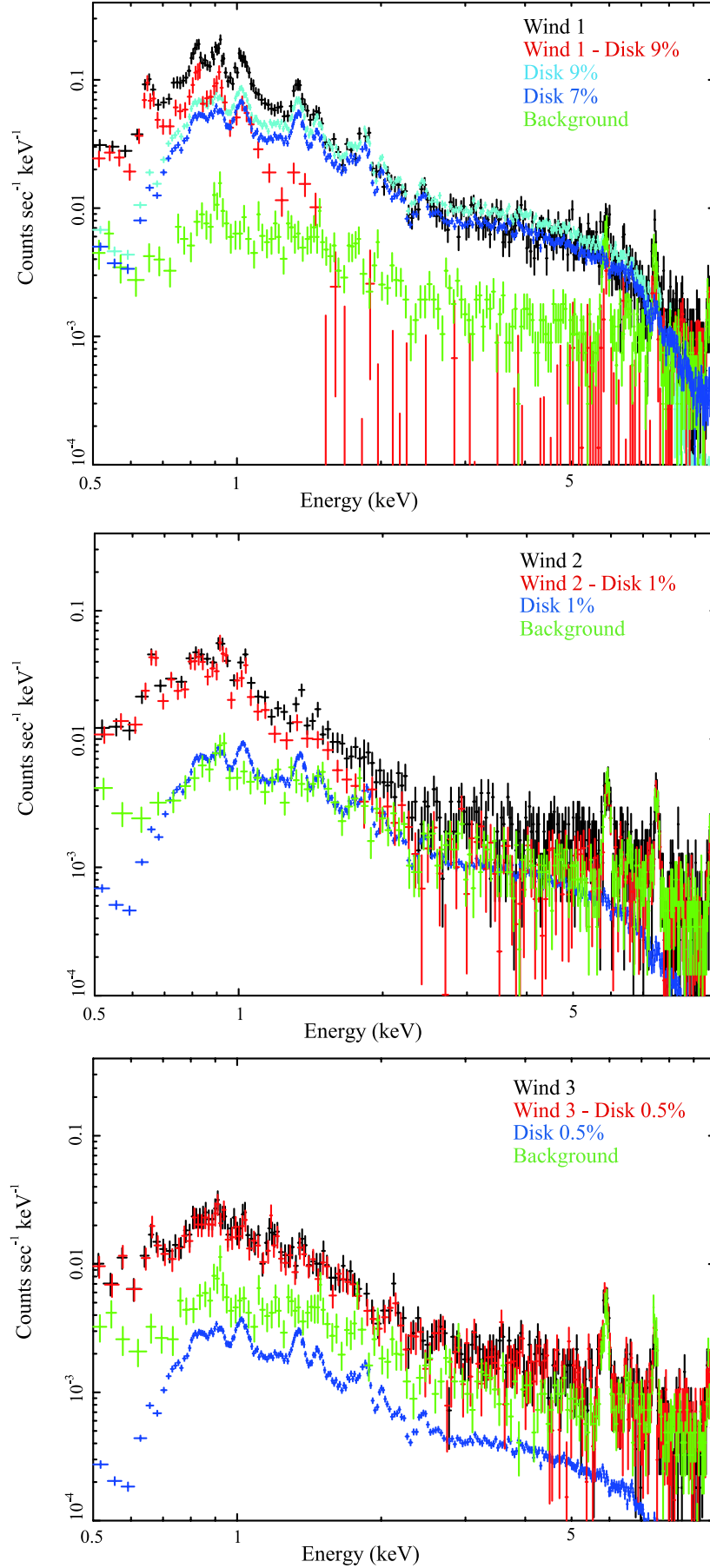


**Fig. 3.** From top to bottom, panels are the comparison spectra between scaled contamination Disk and Wind-1, Wind-2, and Wind-3, respectively. In the top panel, the spectra of Wind-1 and Disk scaled by 9% and 7% are shown in black, light blue, and blue, respectively. The contamination-subtracted Wind-1 and background region spectra are shown as red and green, respectively. The other panels follow the same layout.

**Table 2.** Summary of the best-fit parameters for the Disk region with 3T + Gaussian models.

Parameters		Disk 3T for ISM	Gaussians	Gaussians (contami)
$N_{\text{H}_{\text{M82}}}$	( $10^{20} \text{ cm}^{-2}$ )	$29.9^{+1.22}_{-1.20}$	29.9 (fix)	29.9 (fix)
$kT_{1\text{T}}$	(keV)	$1.93^{+0.11}_{-0.12}$	$1.70^{+0.03}_{-0.08}$	$1.62^{+0.04}_{-0.08}$
$kT_{2\text{T}}$	(keV)	$0.59 \pm 0.01$	$0.61 \pm 0.01$	$0.58 \pm 0.01$
$kT_{3\text{T}}$	(keV)	$0.24 \pm 0.02$	$0.34^{+0.04}_{-0.02}$	$0.08 \pm 0.01$
O	(solar)	$0.45^{+0.05}_{-0.04}$	0 (fix)	0 (fix)
Ne	(solar)	$1.13^{+0.09}_{-0.08}$	0 (fix)	0 (fix)
Mg, Al	(solar)	$1.04 \pm 0.08$	$1.13^{+0.09}_{-0.05}$	$1.09^{+0.06}_{-0.11}$
Si	(solar)	$1.23^{+0.09}_{-0.08}$	$1.23^{+0.09}_{-0.04}$	$1.18^{+0.03}_{-0.05}$
S	(solar)	$1.52 \pm 0.11$	$1.40^{+0.08}_{-0.08}$	$1.38^{+0.07}_{-0.08}$
Ar, Ca	(solar)	$0.65 \pm 0.31$	$1.36^{+0.27}_{-0.26}$	$1.38^{+0.32}_{-0.26}$
Fe, Ni	(solar)	$0.38 \pm 0.03$	$0.42^{+0.05}_{-0.01}$	$0.42^{+0.03}_{-0.04}$
$\Gamma_{\text{cutoff PL}}$		$0.47^{+0.01}_{-0.03}$	$0.52 \pm 0.03$	$0.55^{+0.02}_{-0.04}$
line energy	(keV)	-	0.574 (fix)	0.574 (fix)
Norm	( $10^{-4}$ )	-	$1.28 \pm 0.16$	$1.35^{+0.16}_{-0.15}$
line energy	(keV)	-	0.66 (fix)	0.66 (fix)
Norm	( $10^{-4}$ )	-	$3.34 \pm 0.13$	$3.45^{+0.14}_{-0.13}$
line energy	(keV)	-	0.774 (fix)	0.774 (fix)
Norm	( $10^{-4}$ )	-	$1.08 \pm 0.12$	$1.16 \pm 0.12$
line energy	(keV)	-	0.921 (fix)	0.921 (fix)
Norm	( $10^{-4}$ )	-	$2.24 \pm 0.10$	$6.52^{+0.20}_{-0.10}$
line energy	(keV)	-	$1.03 \pm 0.01$	$1.02 \pm 0.01$
Norm	( $10^{-4}$ )	-	$3.20 \pm 0.09$	$3.22 \pm 0.09$
line energy	(keV)	-	$1.24 \pm 0.01$	$1.24 \pm 0.01$
Norm	( $10^{-4}$ )	-	$0.95 \pm 0.05$	$0.99 \pm 0.05$
$\chi^2/\text{d.o.f.}$		1673/938	1364/933	1293/929

3T model fits result in  $\chi^2/\text{d.o.f.}=479/296$  and  $351/292$ , respectively. In particular, 1T model gives a much worse fit to the data as compared to the 2T model which had a  $\chi^2/\text{d.o.f.}=354/294$ . The derived parameters are summarized in table 3. Furthermore, we calculated confidence contours between the metal abundances (O, Ne, and Mg) relative to Fe, using the 1T, 2T, and 3T ISM models. From these contours, we derived the abundance patterns (table 3), which have smaller uncertainties as compared to the absolute abundance values. Figure 6 shows the abundance patterns of M 82 Wind-1 with 1T, 2T, and 3T models. These metal abundance patterns are consistent within error in all models, although the 3T model shows the largest uncertainties.

#### 4.3. Wind-2 Region

We fitted the Wind-2 region spectra after subtracting 1% of the Disk emission and the background emission accumulated over three background regions with the same model as the Wind-1 region. In this case, the energy ranges are 0.4–5.0 keV for the BI CCD and 0.5–5.0 keV for the FI CCDs. The fit statistic of the 2T model was not good at  $\chi^2/\text{d.o.f.}=397/292$ . Because positive residuals

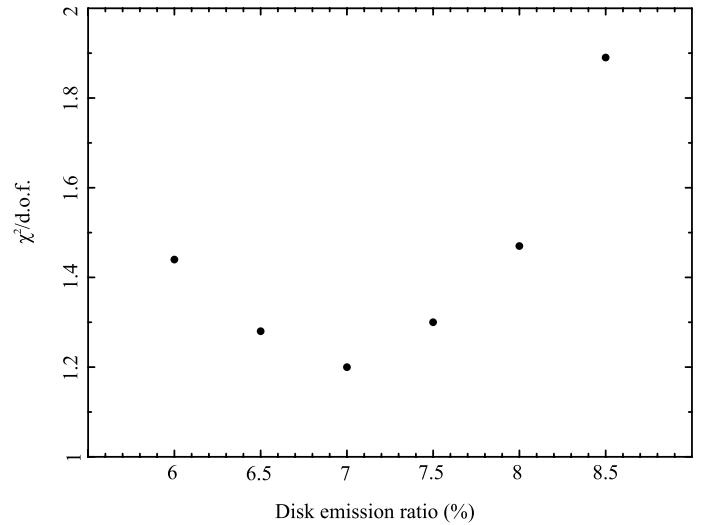


**Fig. 4.** The  $\chi^2/\text{d.o.f.}$  distribution obtained when fitting the Wind-1 spectra, after subtraction of various Disk contamination levels.



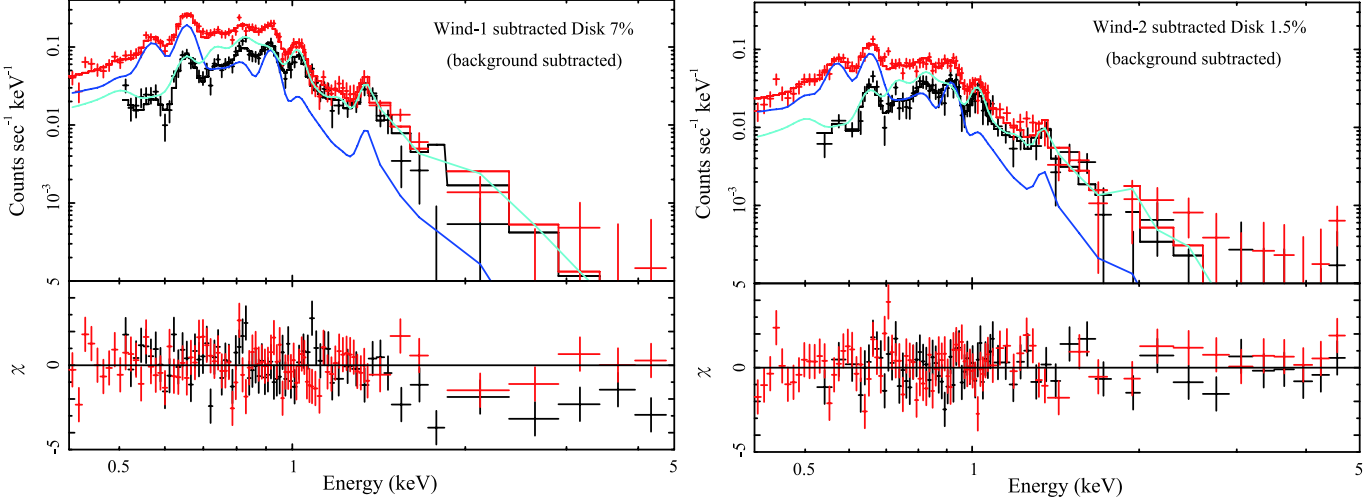


**Fig. 5.** Background-subtracted XIS0 (black) and XIS1 (red) spectra of Wind-1 (left) and Wind-2 (right), shown without removal of instrumental response. Black and red lines show the best-fit model for the XIS0 and XIS1, respectively. For simplicity, only the model components for XIS1 spectra are shown. Blue and light blue lines are the ISM components.

**Table 3.** Summary of the best-fit parameters for the Wind-1 region with 1T, 2T, and 3T for ISM models.

Parameters		Wind-1		
		1T for ISM Disk 7%	2T for ISM	3T for ISM
$N_{\text{H}_G}$	( $10^{20} \text{ cm}^{-2}$ )	4.0 (fix)	4.0 (fix)	4.0 (fix)
$kT_{1T}$	(keV)	$0.38 \pm 0.01$	$0.26 \pm 0.01$	$0.26 \pm 0.01$
$kT_{2T}$	(keV)	-	$0.57 \pm 0.02$	$0.54^{+0.04}_{-0.05}$
$kT_{3T}$	(keV)	-	-	$0.97^{+1.04}_{-0.21}$
O	(solar)	$0.88^{+0.10}_{-0.09}$	$1.00^{+0.17}_{-0.12}$	$0.99^{+0.16}_{-0.13}$
Ne	(solar)	$1.29^{+0.14}_{-0.13}$	$1.73^{+0.29}_{-0.22}$	$1.75^{+0.32}_{-0.26}$
Mg, Al	(solar)	$0.85^{+0.14}_{-0.13}$	$1.09^{+0.23}_{-0.18}$	$1.25^{+0.32}_{-0.24}$
Fe, Ni	(solar)	$0.35 \pm 0.04$	$0.51^{+0.08}_{-0.06}$	$0.60^{+0.14}_{-0.12}$
O/Fe	(solar)	$2.5^{+0.33}_{-0.25}$	$1.96^{+0.32}_{-0.25}$	$1.65^{+1.01}_{-0.40}$
Ne/Fe	(solar)	$3.86^{+0.21}_{-0.36}$	$3.39^{+0.54}_{-0.50}$	$2.93^{+0.74}_{-0.43}$
Mg/Fe	(solar)	$2.5^{+0.28}_{-0.42}$	$2.13^{+0.37}_{-0.30}$	$2.08^{+0.34}_{-0.33}$
$\chi^2/\text{d.o.f.}$		479/296	354/294	351/292

exist above 2 keV, we attempted setting the contamination at 1.5% and 2% intensity of the Disk emission. After subtracting and refitting, we found  $\chi^2/\text{d.o.f.}$  of 360/303 and 668/295, respectively. We accepted 1.5% as the contaminant ratio of Disk emission to Wind-2 region. The resultant parameters and fitted spectra are summarized in table 4 and figure 5, respectively.

In Wind-2 region, we also employed the 1T and 3T models in fitting, assuming that the Disk contamination level is 1.5%. The fitting of 1T and 3T model gives  $\chi^2/\text{d.o.f.}$ =448/305 and 352/301, respectively. Again, the 1T model returns a worse  $\chi^2/\text{d.o.f.}$  of the 2T case 360/303. The metal abundance ratios are derived from confidence contours and are plotted in figure 6. Although the O/Fe ratio of the 3T model is slightly lower than the others, there is no large discrepancy amongst the various

temperature models.

#### 4.4. Wind-3 Region

##### 4.4.1. XMM-Newton Analysis of Source A Spectra

Before fitting the Wind-3 spectra, we estimate the emission from Source A based upon XMM-Newton data. We extracted source spectra within a  $15''$  radius circular aperture centered at  $(\alpha, \delta) = (09^{\text{h}}55^{\text{m}}14^{\text{s}}, +69^{\circ}47'35'')$ . The background spectra were extracted from an annular ring and subtracted from Source A. We extracted the spectra of MOS 1, MOS 2, and PN and fitted these simultaneously in the 0.3–7.0 keV energy range with the following model;  $\text{phabs}_A \times \text{PL}_A$ , with all parameters set free. The best fit values are listed in table 5. The Source A spectra are reproduced by the absorbed PL model with a photon index of  $1.76^{+0.10}_{-0.09}$ , which is consistent with a typical active



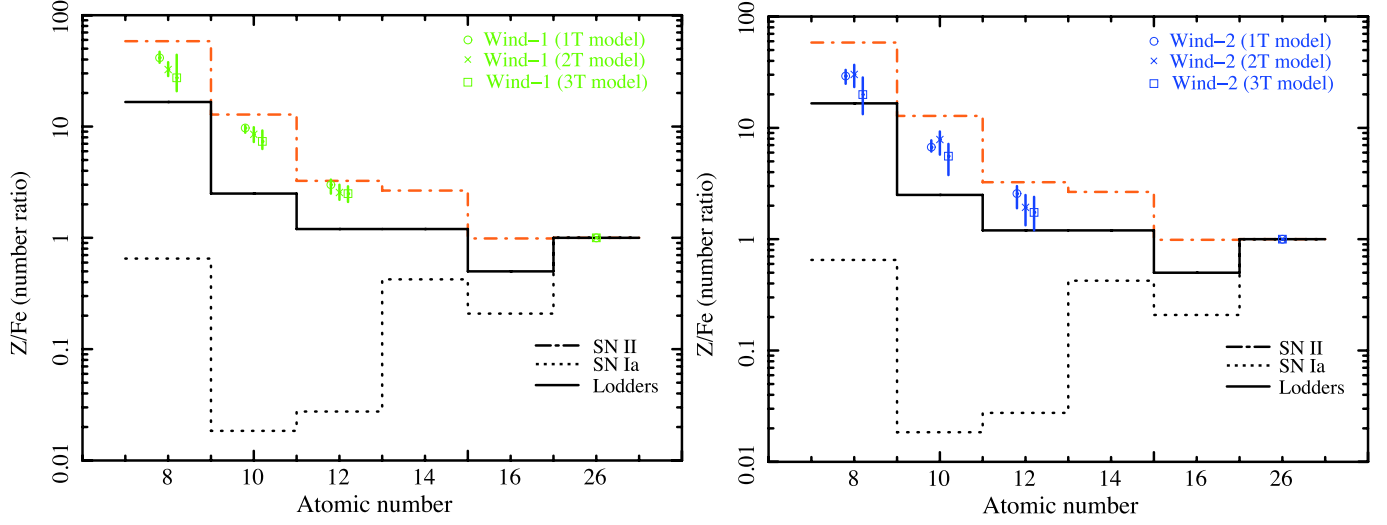


**Fig. 6.** Abundance ratios of O, Ne, and Mg to Fe for the 1T, 2T, and 3T model of the M 82 Wind-1 (left) and Wind-2 (right) regions. The abundance patterns of Wind-1 and Wind-2 region are also shown. Solid, dot-dashed, and dotted lines represent the number ratios of metals to Fe for the solar abundance, for SN II, and for SN Ia products (Lodders 2003; Iwamoto et al. 1999; Nomoto et al. 2006), respectively.

**Table 4.** Summary of the best-fit parameters for the Wind-2 region with 1T, 2T, and 3T for ISM models.

Parameters		Wind-2		
		1T for ISM Disk 1.5%	2T for ISM	3T for ISM
$N_{\text{H}_G}$	( $10^{20} \text{ cm}^{-2}$ )	4.0 (fix)	4.0 (fix)	4.0 (fix)
$kT_{1T}$	(keV)	$0.32 \pm 0.01$	$0.24 \pm 0.01$	$0.24 \pm 0.01$
$kT_{2T}$	(keV)	-	$0.53^{+0.06}_{-0.05}$	$0.50^{+0.08}_{-0.06}$
$kT_{3T}$	(keV)	-	-	$1.18^{+0.47}_{-0.25}$
O	(solar)	$0.61^{+0.09}_{-0.07}$	$0.69^{+0.12}_{-0.10}$	$0.69^{+0.13}_{-0.10}$
Ne	(solar)	$0.94^{+0.15}_{-0.12}$	$1.20^{+0.23}_{-0.19}$	$1.28^{+0.31}_{-0.25}$
Mg, Al	(solar)	$0.70^{+0.20}_{-0.17}$	$0.62^{+0.21}_{-0.17}$	$0.84^{+0.38}_{-0.27}$
Fe, Ni	(solar)	$0.34^{+0.06}_{-0.05}$	$0.38^{+0.08}_{-0.06}$	$0.57^{+0.21}_{-0.15}$
O/Fe	(solar)	$1.76^{+0.24}_{-0.26}$	$1.82^{+0.40}_{-0.42}$	$1.2^{+0.51}_{-0.40}$
Ne/Fe	(solar)	$2.67^{+0.41}_{-0.23}$	$3.13^{+0.57}_{-0.84}$	$2.22^{+0.64}_{-0.72}$
Mg/Fe	(solar)	$2.14^{+0.36}_{-0.56}$	$1.61^{+0.47}_{-0.50}$	$1.45^{+0.55}_{-0.45}$
$\chi^2/\text{d.o.f.}$		448/305	360/303	352/301

**Table 5.** Best-fit parameters for Source A with  $\text{phabs}_A \times \text{PL}_A$ 

Parameters		
$N_{\text{H}_A}$	$(10^{20} \text{ cm}^{-2})$	$11.2^{+2.20}_{-2.44}$
$\Gamma_A$		$1.76^{+0.10}_{-0.09}$
Source A flux*	$(\text{erg cm}^{-2} \text{ s}^{-1})$	$2.2^{+0.3}_{-0.2} \times 10^{-13}$
$\chi^2/\text{d.o.f.}$		167/178

\* Flux within the accumulated region between 0.5 and 8 keV.

galactic nucleus spectrum.

#### 4.4.2. Estimation of Background Emission

As a result of lower surface brightness of the Wind-3 region as compared to Wind-1 and Wind-2 (figure 3), we decided to perform simultaneous fitting of the Wind-3 and background spectra. Background spectra were extracted from three regions. Because the NXB is subtracted, the background components consist of Cosmic X-ray Background (CXB) and Galactic thermal emission. We represented CXB with a PL model and Galactic thermal emission as a two-temperature apec model (Smith et al. 2001). Empirically, one thermal component represents the sum of solar wind charge exchange (SWCX) and local hot bubble (LHB), while Milky Way halo (MWH) emits the other thermal component (Yoshino et al. 2009).

We fitted the spectra with the following models;  $\text{phabs}_G \times (\text{PL}_{\text{CXB}} + \text{apec}_{\text{MWH}}) + \text{apec}_{\text{LHB}}$ . The ‘ $\text{phabs}_G$ ’ model represents the photoelectric absorption, whose column density was fixed to the Galactic value of  $4.0 \times 10^{20} \text{ cm}^{-2}$  in the direction of M 82. The ‘ $\text{apec}_{\text{MWH}}$ ’ and ‘ $\text{apec}_{\text{LHB}}$ ’ models correspond to thermal emission from our Galaxy, with the metal abundances fixed at the solar value and zero redshift. The spectra from the BI and FI CCDs were simultaneously fitted in the 0.4–5.0 and 0.5–5.0 keV range, respectively. In table 6, we list the derived parameters, which are consistent with Tsuru et al. (2007). This model reproduced the spectra approximately, with  $\chi^2/\text{d.o.f.} = 312/255$ . The derived photon index of  $\text{PL}_{\text{CXB}}$  is  $1.43^{+0.09}_{-0.11}$ , which is consistent with Kushino et al. (2002). Although the temperature of  $\text{apec}_{\text{MWH}}$  model is higher than that of the common MWH component ( $\sim 0.25$  keV), there are known to be high temperature Galactic component ( $\sim 0.6$  keV) present in some portions of the sky (Yoshino et al. 2009). Furthermore, similar results are reported in Sato et al. (2008) and Konami et al. (2010). Since the Galactic emission is considered to have spatial dependencies, we regard this model to be appropriate for estimating the background emission in this analysis.

#### 4.4.3. Simultaneously Fitting of Wind-3 and Background Regions

We fitted the Wind-3 spectra and background simultaneously with following models;  $\text{phabs}_G \times \text{vapec}_{1\text{T},2\text{T}} + \text{phabs}_A \times \text{PL}_A + \text{background models}$ . Here, we used energies ranging from 0.4 (BI) or 0.5 (FI) to 5.0 and 8.0 keV for the background and Wind-3 regions, respectively. The first and second terms represent the outflow and Source-A, respectively. The photon index of the PL model for

**Table 6.** Best-fit parameters for the background regions with apec components + PL model.\*

Parameters		
$N_{\text{H}_G}$	$(10^{20} \text{ cm}^{-2})$	4.0 (fix)
$\Gamma_{\text{CXB}}$		$1.43^{+0.09}_{-0.11}$
$kT_{\text{MWH}}$	(keV)	$0.70 \pm 0.07$
Abundance	(solar)	1 (fix)
$kT_{\text{LHB}}$	(keV)	$0.21^{+0.03}_{-0.02}$
Abundance	(solar)	1 (fix)
$\text{Norm}_{\text{LHB}}/\text{Norm}_{\text{MWH}}$		$0.97^{+0.12}_{-0.19}$
$\chi^2/\text{d.o.f.}$		312/255

\* The apec components for spectra in the background region of M 82 with absorbed MWH component, LHB component for the Galactic emission, and a PL model for CXB.

CXB was fixed to 1.43, which was best fit parameter in section 4.4.2. All the other background parameters were linked between the two regions.

We employed the 1T and 2T models in fitting, and found  $\chi^2/\text{d.o.f.} = 601/543$  and  $587/541$ , respectively. The fitted spectra and derived parameters are shown in figure 7 and table 7, respectively. The temperatures and metal abundances between the 1T and 2T models are consistent with each other, although the 2T model allows higher values of abundances. When employing the 3T model, the third temperature could not be constrained and the normalization is less than 10% of the those of other components. The spectra of Wind-3 region do not require a third temperature component.

#### 4.5. Search for CX emission in Wind regions

As seen in section 3.2, the CX emission may contribute in addition to thermal emission in Disk region. To search for CX emission in Wind regions, we fitted the spectra of Wind-1, Wind-2, and Wind-3 regions with a 2T thermal model including six Gaussians representing O and Ne emission lines, by setting O and Ne abundance of vapec models to zero, as described in section 3.2. The ratios of  $(\text{O VII K}\beta + \text{O VIII Ly}\alpha)/\text{O VII K}\alpha$ ,  $\text{O VIII Ly}\beta/(\text{O VII K}\beta + \text{O VIII Ly}\alpha)$ ,  $(\text{Ne IX K}\beta + \text{Ne X Ly}\alpha)/\text{Ne IX K}\alpha$ , and  $\text{Ne X Ly}\beta/(\text{Ne IX K}\beta + \text{Ne X Ly}\alpha)$  are derived in Disk, Wind-1, Wind-2, and Wind-3 regions.

## 5. Discussion

### 5.1. Excess emission of Ly $\beta$ lines of H-like O and Ne

There are residual structures at 0.5–0.7 keV and  $\sim 1.2$  keV in the spectra of the Disk region fitted with the thermal models. These residuals are well fitted by excess emission of Ly $\beta$  lines of O VIII and Ne X. A plausible explanation for these residuals is CX between highly ionized O/Ne and neutral H/He, since the CX process gives higher ratios of  $\text{K}\beta/\text{K}\alpha$  or  $\text{K}\gamma/\text{K}\beta$  than those of CIE plasma. We calculated confidence contours between the normalizations of the Gaussian lines,  $\text{O VIII Ly}\beta/(\text{O VII K}\beta + \text{O VIII Ly}\alpha)$  and  $\text{Ne X Ly}\beta/(\text{Ne IX K}\beta + \text{Ne X Ly}\alpha)$ , us-

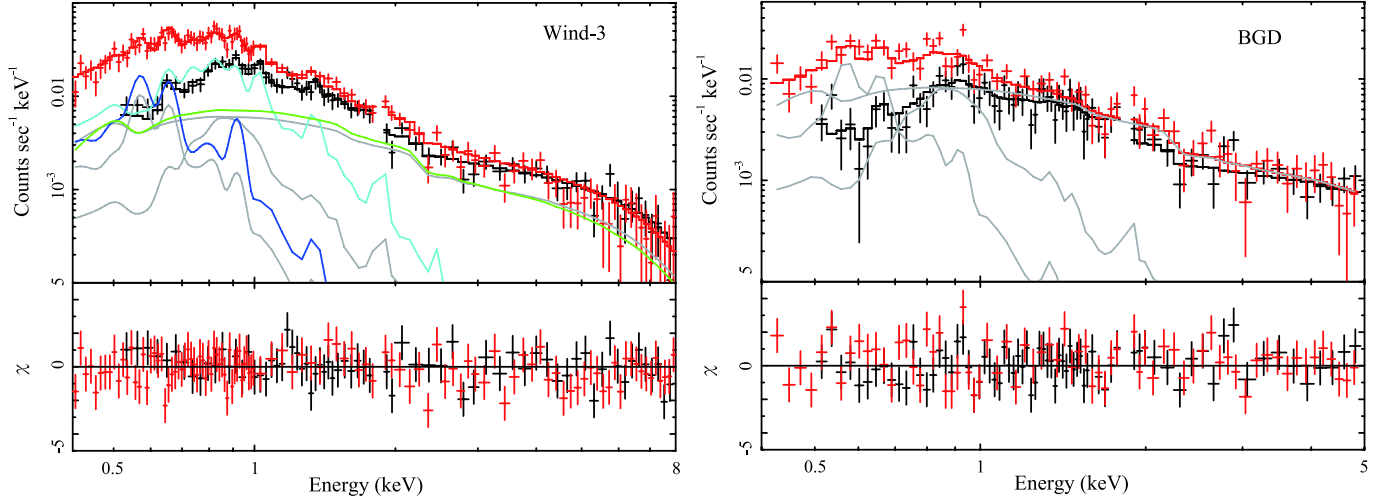


**Fig. 7.** NXB-subtracted XIS0 (black) and XIS1 (red) spectra of M82 (left panel), and those of the background region (right panel), shown without removal of instrumental response. The left panel employs the two-temperature model for the ISM. Black and red lines show the best-fit model for XIS0 and XIS1, respectively. For simplicity, only the model components for XIS1 spectra are shown. Blue and light blue lines are the ISM components, the green line is emission from Source A modelled as an absorbed power-law ( $PL_A$ ), gray lines are the Galactic background emission ( $apec_{MWH}$  and  $apec_{LHB}$ ) and the CXB components, respectively. The background components are common between the on-source and background spectra, but scaled to the respective data accumulation area.

**Table 7.** Summary of the best-fit parameters for the Wind-3 region with 1T or 2T for ISM models.

Parameters		Wind-3	
		1T for ISM	2T for ISM
$N_{HG}$	( $10^{20} \text{ cm}^{-2}$ )	4.0 (fix)	4.0 (fix)
$kT_{1T}$	(keV)	$0.41^{+0.05}_{-0.03}$	$0.20^{+0.04}_{-0.06}$
$kT_{2T}$	(keV)	-	$0.49^{+0.08}_{-0.09}$
$Norm_{1T}/Norm_{2T}$		-	$0.53^{+0.72}_{-0.35}$
O	(solar)	$0.57^{+0.27}_{-0.17}$	$0.68^{+0.55}_{-0.26}$
Ne	(solar)	$0.95^{+0.44}_{-0.24}$	$1.48^{+1.21}_{-0.47}$
Mg, Al	(solar)	$0.61^{+0.25}_{-0.23}$	$0.90^{+0.64}_{-0.34}$
Fe, Ni	(solar)	$0.21^{+0.12}_{-0.07}$	$0.31^{+0.31}_{-0.07}$
O/Fe	(solar)	$2.73^{+1.66}_{-0.98}$	$2.17^{+0.77}_{-0.97}$
Ne/Fe	(solar)	$4.55^{+1.70}_{-1.30}$	$4.84^{+1.98}_{-1.46}$
Mg/Fe	(solar)	$2.90^{+1.39}_{-1.15}$	$2.90^{+1.10}_{-1.15}$
<hr/>			
$N_{HA}$	( $10^{20} \text{ cm}^{-2}$ )	11.2 (fix)	11.2 (fix)
$\Gamma_A$		$1.73^{+0.23}_{-0.16}$	$1.68^{+0.23}_{-0.16}$
Source A flux*	( $\text{erg cm}^{-2} \text{ s}^{-1}$ )	$2.1^{+0.5}_{-0.2} \times 10^{-13}$	$2.1^{+0.61}_{-0.39} \times 10^{-13}$
<hr/>			
$\chi^2/\text{d.o.f.}$		601/543	587/541

\* Flux within the accumulated region between 0.5 and 8 keV.

ing thermal models including six Gaussians representing O and Ne emission lines (see subsection 3.2). In figure 8, the derived these values are plotted against plasma temperature with those of the CIE plasma from the APEC code. Both these ratios for H-like O and Ne in the Disk region have values of  $\sim 0.3$ , significantly larger than those predicted for the CIE plasma. Since the temperature dependence of  $\text{Ly}\beta$  to  $\text{Ly}\alpha$  ratio is relatively small, no combination of temperature components alone can give the observed high  $\text{Ly}\beta$  excess. In contrast, the Wind regions have ratios of  $\text{O VIII Ly}\beta/(\text{O VII K}\beta + \text{O VIII Ly}\alpha)$  and  $\text{Ne X Ly}\beta/(\text{Ne IX K}\beta + \text{Ne X Ly}\alpha)$  which are consistent with those for the CIE plasma. Especially, in the Wind-1 region,  $\text{O VIII Ly}\beta/(\text{O VII K}\beta + \text{O VIII Ly}\alpha)$  is factor of 3–10 smaller than those in the Disk region. Therefore, this line ratio analysis indicates that the CX process gives higher  $\text{Ly}\beta$  to  $\text{Ly}\alpha$  ratio of H-like O and Ne in the Disk region.

For He-like ions, the values of  $(\text{O VII K}\beta + \text{O VIII Ly}\alpha)/\text{O VII K}\alpha$  and  $(\text{Ne IX K}\beta + \text{Ne X Ly}\alpha)/\text{Ne IX K}\alpha$  in the Disk and the all Wind regions are consistent with those of CIE plasma. The cross-sections of interaction of highly ionized H-like ions with neutral H/He atoms are larger than those of He-like ions (Koutroumpa et al. 2006 and references therein). Since  $\text{K}\beta$  line energies of He-like O and Ne are close to those of  $\text{K}\alpha$  lines of H-like ions of the same element, and since the ratios of He-like to H-like ion  $\text{K}\alpha$  lines have very steep temperature dependencies,  $\text{K}\beta$  to  $\text{K}\alpha$  ratios of He-like ions are not suitable for the study of the contribution of CX emission using CCD spectra.

The  $\text{Ly}\beta$  lines of H-like O and Ne lie close the expected energies of strong Fe-L lines. Large residuals at  $\sim 1.2$  keV have been observed in various kinds of objects (e.g. Yamaguchi et al. 2010). In elliptical galaxies with hot ISM of  $\sim 0.6$  keV, residuals at  $\sim 0.8$  keV are also observed (Matsushita et al. 2007; Tawara et al. 2008). These residuals have been interpreted as a problem in the Fe-L atomic data (e.g. Brickhouse et al. 2000). However, there is a clear difference in the residual structures between the Disk and the Wind-1 regions of M 82. In these two regions, the O and Ne lines mostly come from the same two temperature components, 0.2–0.3 keV and  $\sim 0.6$  keV, although the ratio of the normalization is different. Therefore, this spatial variation of the residual structure indicates the difference to be a result of CX rather than uncertainties in the Fe-L atomic data.

Liu et al. (2011) discovered excess emission of the forbidden lines in the triplet of the He-like O and Ne, which are robust evidence of CX. They assumed the temperature of thermal emission is  $\sim 0.6$  keV, which is derived using the ratio of  $\text{Mg XII Ly}\alpha/\text{Mg XI K}\alpha$ . Therefore, the CX emission of O VII is a result of the capture of two electrons by O IX ions, while the cross-section of this process is less than 20% of that of single-electron capture via the CX process of O VIII, because the ion fraction of O IX is dominant at the  $\sim 0.6$  keV CIE plasma (Liu et al. 2011, Greenwood et al. 2001). Liu et al. (2011) evaluated the contribution of CX to be  $\sim 90\%$  to the O VII triplet, assuming the temperature of thermal emission to be  $\sim 0.4$ – $0.6$  keV. The contri-

bution of CX depends on the temperature structure, since the fraction of resonance, intercombination, and forbidden lines are dependent on the plasma temperature (Porquet & Dubau 2000). The ISM of galaxies is empirically assumed to be composed of a multiple temperature plasma. In fact, our results need  $\sim 0.2$  keV temperature plasma for the disk emission, which accounts for  $\sim 30\%$  of the He-like triplet of O. The existence of the 0.2 keV plasma increases the ratio of the forbidden to resonance lines, but this is still much smaller than the observed values in Liu et al. (2011). With Astro-H, next Japanese X-ray satellite, we will be able to resolve these  $\text{K}\alpha$  and  $\text{K}\beta$  lines of H-like and He-like ions, as well as the triplets of He-like lines, and investigate CX more clearly.

CX should strongly contribute to the X-ray emission in the central regions of starburst galaxies, where abundant cold gas and highly ionized ions co-exist and interact. We have detected plausible evidence of CX emission between H-like ions (O and Ne) and neutrals (H and He) in the Disk region. In the ‘cap’ region, the ionized outflow from M 82 are thought to collide with cool ambient gas and enhance the  $\text{H}\alpha$  and X-ray emission, and may also cause CX emission (e.g. Devine & Bally 1999, Lehnert 1999). An emission line consistent with the C VI transition of  $n = 4$  to 1 at 0.459 keV has been marginally detected, although it is not statistically significant at the 99% confidence level (Tsuru et al. 2007).

## 5.2. Metal Abundance Patterns of All Wind regions

We have successfully derived metal abundances of O, Ne, Mg, and Fe over the entire Wind region of M 82 for the first time. The spectra are well reproduced with thermal models and without evidence of CX emission in the outflow regions. In these regions, the amount of neutral gas may be smaller than those in the Disk and ‘cap’ regions, and therefore, the effect of the CX may not be important. As a result, the metal abundances in the Wind regions should be more reliable than those in the Disk and ‘cap’ regions. Furthermore, there no discrepancies among the metal abundance ratios determined using either the 1T, 2T, or 3T ISM model over all the Wind regions. We calculated confidence contours between the abundance of metals (O, Ne, and Mg) relative to Fe, using the 2T model for ISM of all Wind regions. From these contours, we derived the abundance patterns (table 3, table 4, and table 7), which have smaller uncertainties as compared to the absolute abundance values. Figure 9 shows the abundance patterns of M 82 Wind-1, Wind-2, and Wind-3 within the ‘cap’ region (Tsuru et al. 2007). The distance of these regions from the galactic center range from 2 kpc to 10 kpc. The O/Fe, Ne/Fe, and Mg/Fe ratios are consistent with no spatial variation.

The calculated SN II and SN Ia yields are also plotted in figure 9. The SN II yields by Nomoto et al. (2006) refer to an average over the Salpeter initial mass function of stellar mass from 10 to  $50 M_{\odot}$ , with a progenitor metallicity of  $Z = 0.02$ . The SN Ia yields were taken from the W7 model Iwamoto et al. (1999). The O/Fe, Ne/Fe, and Mg/Fe ratios are a factor of 2–3 higher than the solar values, and

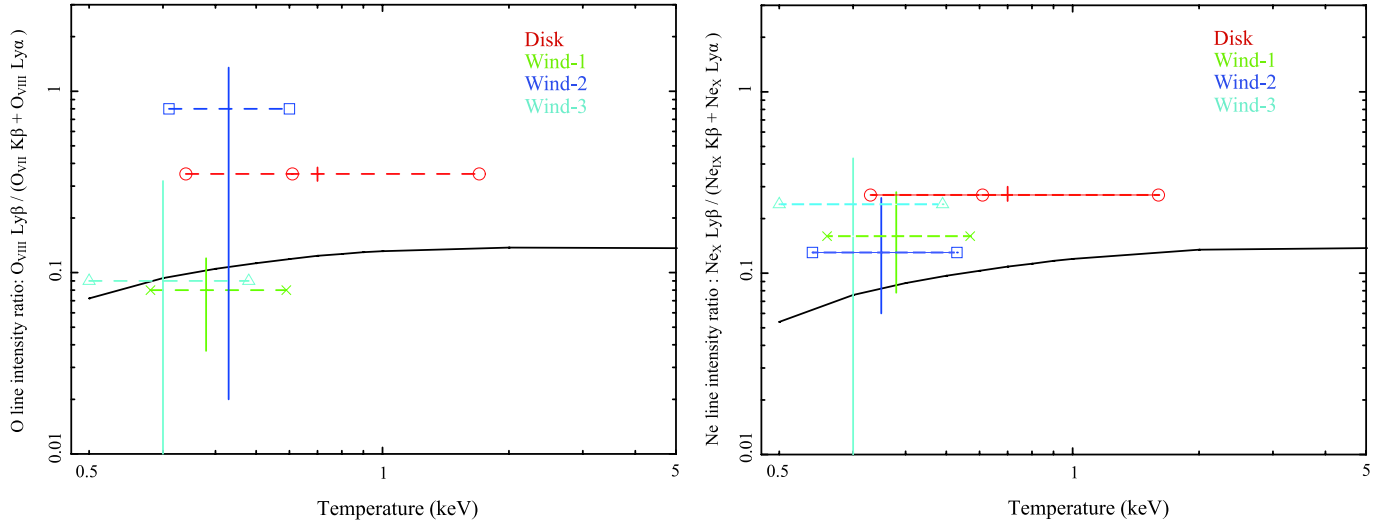


**Fig. 8.** Left; The red, green, blue, and light blue data represent the values of the line intensity ratio  $O\text{ VIII Ly}\beta / (O\text{ VII K}\beta + O\text{ VIII Ly}\alpha)$  vs. the thermal model temperatures, for the Disk, Wind-1, Wind-2, and Wind-3 regions, respectively. The temperatures used are those determined from thermal models including six Gaussians representing O and Ne emission lines, by setting O and Ne abundance of vepc models to zero. The solid line is same ratio predicted for a CIE plasma using the vepc code (Smith et al. 2001). Right; Symbols and curves are as in the left-hand panel, but for the line ratio  $Ne\text{ X Ly}\beta / (Ne\text{ IX K}\beta + Ne\text{ X Ly}\alpha)$ .

therefore, the outflow of M 82 is significant enriched by SN II yields. The outflow wind of another starburst galaxy, NGC 4631, observed with Suzaku also shows enhancements of  $\alpha$ -elements relative to the Fe abundance ratios (Yamasaki et al. 2009), although its disk region possesses a hot ISM with an approximately solar abundance pattern. The abundance pattern of the hot ISM in NGC 4258, a spiral galaxy without starburst activity, is also consistent with the solar ratio (Konami et al. 2009). These results indicate that starburst galaxies eject metals synthesized by SN II into the intergalactic medium via outflows. The derived abundance pattern of the Disk region, especially the very low O abundance relative to the other elements, is similar to those observed with ASCA and XMM (Tsuru et al. 1997; Ranalli et al. 2008). However, the observed excess emission of  $Ly\beta$  lines and forbidden lines in He-like triplet indicates that a significant fraction of these lines are caused by CX process. Therefore, it is very difficult to isolate the thermal emission owing to the multiple temperature ISM plasma. Furthermore, the derived value of  $N_H$ ,  $\sim 30 \times 10^{20} \text{ cm}^{-2}$ , is significantly higher than the Galactic value of  $\sim 4 \times 10^{20} \text{ cm}^{-2}$ , whereas those of the Wind regions are consistent to the Galactic value. The observed value of  $N_H$  toward the Disk region means that 85% of photons in the  $Ly\alpha$  line of H-like O must be absorbed, while only 20-30% of K lines of Mg absorbed. The cold gas which absorbs the X-ray emission from the Disk should be non-uniform, and X-ray photons should be partially absorbed. Therefore, the observed very low abundance of O may be caused by incorrect modelling of spectral components of this very complicated plasma in the Disk region.

## 6. Conclusion

We have performed X-ray spectral analysis of the outflow region of M 82 observed with Suzaku. Suzaku XIS has a high spectral sensitivity to faint O lines thanks to a very small low-pulse-height tail below  $\sim 1$  keV. The spectra from the galactic disk are reproduced with 3T thermal models and excess emission of  $Ly\beta$  lines of O VIII and Ne X, which may be caused by CX process. In the outflow region, there is no excess  $Ly\beta$  emission, and the derived O/Fe, Ne/Fe, and Mg/Fe ratios are a factor of 2–3 higher than the solar ratio. This abundance pattern indicates that starburst activity enriches the intergalactic medium with SN II yields via outflows.

We thank the referee for providing valuable comments. We gratefully acknowledge all members of the Suzaku hardware and software teams and the Science Working Group. SK is supported by JSPS Research Fellowship for Young Scientists.

## References

- Bauer, M., Pietsch, W., Trinchieri, G., Breitschwerdt, D., Ehle, M., & Read, A. 2007, *A&A*, 467, 979
- Brickhouse, N. S., Dupree, A. K., Edgar, R. J., Liedahl, D. A., Drake, S. A., White, N. E., & Singh, K. P. 2000, *ApJ*, 530, 387
- Cox, D. P. 1998, *IAU Colloq. 166: The Local Bubble and Beyond*, 506, 121
- Cravens, T. E. 2000, *ApJL*, 532, L153
- Devine, D., & Bally, J. 1999, *ApJ*, 510, 197
- Fujimoto, R., et al. 2007, *PASJ*, 59, 133
- Greenwood, J. B., Williams, I. D., Smith, S. J., & Chutjian, A. 2001, *Phys. Rev. A*, 63, 062707
- Ishisaki, Y., et al. 2007, *PASJ*, 59, 113

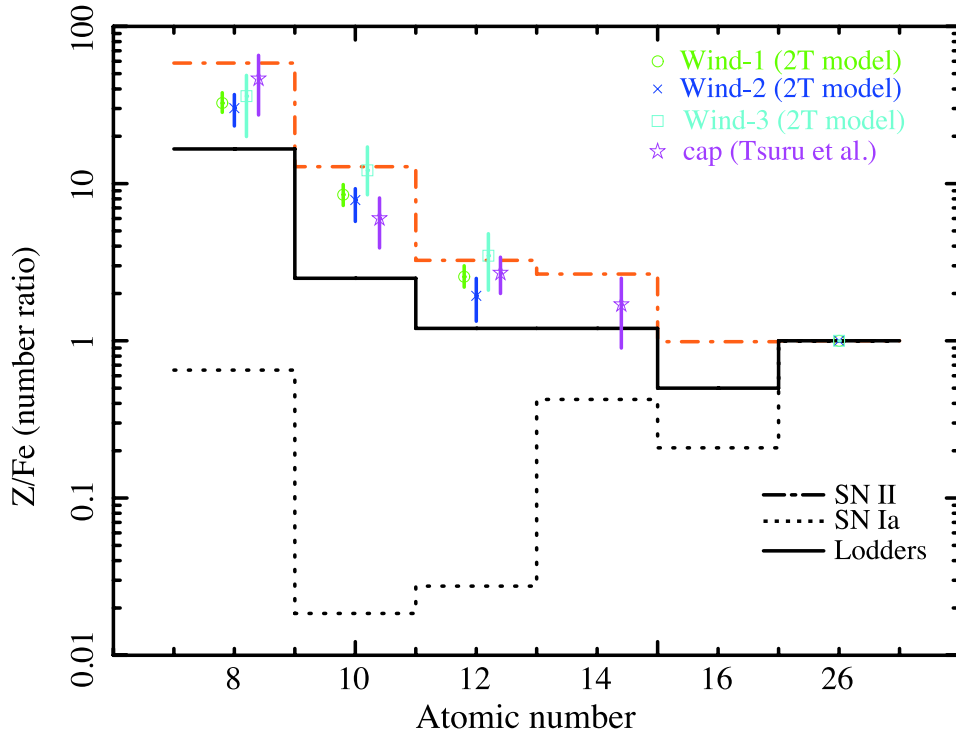


**Fig. 9.** Abundance ratios of O, Ne, and Mg to Fe for the best-fit model of the M 82 Wind regions. The abundance patterns of Wind-1 (green), Wind-2 (blue), Wind-3 (light blue), and cap (magenta; Tsuru et al. 2007) regions are also shown. Solid, dot-dashed, and dotted lines represent the number ratios of metals to Fe for the solar abundance, for SN II, and for SN Ia products (Lodders 2003; Iwamoto et al. 1999; Nomoto et al. 2006), respectively.

- Iwamoto, K., Brachwitz, F., Nomoto, K., Kishimoto, N., Umeda, H., Hix, W. R., & Thielemann, F.-K. 1999, *ApJS*, 125, 439
- Karachentsev, I. D., Karachentseva, V. E., Huchtmeier, W. K., & Makarov, D. I. 2004, *AJ*, 127, 2031
- Katsuda, S., et al. 2011, *ApJ*, 730, 24
- Konami, S., et al. 2009, *PASJ*, 61, 941
- Konami, S., Matsushita, K., Nagino, R., Tashiro, M. S., Tamagawa, T., & Makishima, K. 2010, *PASJ*, 62, 1435
- Koutroumpa, D., Lallement, R., Kharchenko, V., Dalgarno, A., Pepino, R., Izmodenov, V., & Quémerais, E. 2006, *A&A*, 460, 289
- Koyama, K., et al. 2007, *PASJ*, 59, 23
- Kushino, A., Ishisaki, Y., Morita, U., Yamasaki, N. Y., Ishida, M., Ohashi, T., & Ueda, Y. 2002, *PASJ*, 54, 327
- Lallement, R. 2004, *A&A*, 422, 391
- Lehnert, M. D. 1999, *Wolf-Rayet Phenomena in Massive Stars and Starburst Galaxies*, 193, 645
- Lisse, C. M., et al. 1996, *Science*, 274, 205
- Liu, J., Wang, Q. D., Li, Z., & Peterson, J. R. 2010, *MNRAS*, 404, 1879
- Liu, J., Mao, S., & Wang, D. 2011, *arXiv:1105.3539*
- Lodders, K. 2003, *ApJ*, 591, 1220
- Matsushita, K., et al. 2007, *PASJ*, 59, 327
- Miyawaki, R., Makishima, K., Yamada, S., Gandhi, P., Mizuno, T., Kubota, A., Tsuru, T. G., & Matsumoto, H. 2009, *PASJ*, 61, 263
- Nomoto, K., Tominaga, N., Umeda, H., Kobayashi, C., Origlia, L., Ranalli, P., Comastri, A., & Maiolino, R. 2004, *ApJ*, 606, 862 & Maeda, K. 2006, *Nuclear Physics A*, 777, 424
- Porquet, D., & Dubau, J. 2000, *A&AS*, 143, 495
- Ranalli, P., Comastri, A., Origlia, L., & Maiolino, R. 2008, *MNRAS*, 386, 1464
- Rasmussen, A. P., Behar, E., Kahn, S. M., den Herder, J. W., & van der Heyden, K. 2001, *A&A*, 365, L231
- Sato, K., et al. 2007, *PASJ*, 59, 299
- Serlemitsos, P. J., et al. 2007, *PASJ*, 59, 9
- Smith, R. K., Brickhouse, N. S., Liedahl, D. A., & Raymond, J. C. 2001, *ApJL*, 556, L91
- Stevens, I. R., Read, A. M., & Bravo-Guerrero, J. 2003, *MNRAS*, 343, L47
- Strickland, D. K., & Heckman, T. M. 2007, *ApJ*, 658, 258
- Strickland, D. K. 2007, *MNRAS*, 376, 523
- Tawa, N., et al. 2008, *PASJ*, 60, 11
- Tawara, Y., Matsumoto, C., Tozuka, M., Fukazawa, Y., Matsushita, K., & Anabuki, N. 2008, *PASJ*, 60, 307
- Tsuru, T. G., Awaki, H., Koyama, K., & Ptak, A. 1997, *PASJ*, 49, 619
- Tsuru, T. G., et al. 2007, *PASJ*, 59, 269
- Wang, Q. D., Whitaker, K. E., & Williams, R. 2005, *MNRAS*, 362, 1065
- Wang, J., Fabbiano, G., Elvis, M., Risaliti, G., Mazzarella, J. M., Howell, J. H., & Lord, S. 2009, *ApJ*, 694, 718
- Yamasaki, N. Y., Sato, K., Mitsuishi, I., & Ohashi, T. 2009, *PASJ*, 61, 291
- Yamaguchi, H., Sawada, M., & Bamba, A. 2010, *ApJ*, 715, 412
- Yoshino, T., et al. 2009, *PASJ*, 61, 805